UNIVERSITY OF AMSTERDAM

UvA-DARE (Digital Academic Repository)

Impact of accretion assumptions on pulse profile modelling of superburst oscillations in 4U 1636-536

Kini, Yves; Watts, Anna L.; Salmi, Tuomo; Bilous, Anna; Vinciguerra, Serena; Guillot, Sebastien; Ballantyne, David R.; Kuulkers, Erik; Bogdanov, Slavko; Suleimanov, Valery

DOI
10.1093/mnras/staf908

Publication date
2025

Document Version
Final published version

Published in
Monthly Notices of the Royal Astronomical Society

License
CC BY

Link to publication

Citation for published version (APA):
Kini, Y., Watts, A. L., Salmi, T., Bilous, A., Vinciguerra, S., Guillot, S., Ballantyne, D. R., Kuulkers, E., Bogdanov, S., & Suleimanov, V. (2025). Impact of accretion assumptions on pulse profile modelling of superburst oscillations in 4U 1636-536. *Monthly Notices of the Royal Astronomical Society*, *541*(1), 46-57. https://doi.org/10.1093/mnras/staf908

General rights
It is not permitted to download or to forward/distribute the text or part of it without the consent of the author(s) and/or copyright holder(s), other than for strictly personal, individual use, unless the work is under an open content license (like Creative Commons).

Disclaimer/Complaints regulations
If you believe that digital publication of certain material infringes any of your rights or (privacy) interests, please let the Library know, stating your reasons. In case of a legitimate complaint, the Library will make the material inaccessible and/or remove it from the website. Please Ask the Library: https://uba.uva.nl/en/contact, or a letter to: Library of the University of Amsterdam, Secretariat, P.O. Box 19185, 1000 GD Amsterdam, The Netherlands. You will be contacted as soon as possible.
UvA-DARE is a service provided by the library of the University of Amsterdam (https://dare.uva.nl)

Download date:11 Nov 2026

Monthly Notices of the ROYAL ASTRONOMICAL SOCIETY

MNRAS **541,** 46–57 (2025) https://doi.org/10.1093/mnras/staf908
Advance Access publication 2025 June 4

Impact of accretion assumptions on pulse profile modelling of superburst oscillations in 4U 1636−536

Yves Kini [1★] Anna L. Watts [1] Tuomo Salmi [1,2] Anna Bilous [3] Serena Vinciguerra [1] Sebastien Guillot [4,5] David R. Ballantyne [6] Erik Kuulkers [7] Slavko Bogdanov [8] and Valery Suleimanov [9]

[1]*Anton Pannekoek Institute for Astronomy, University of Amsterdam, Science Park 904, NL-1098 XH Amsterdam, the Netherlands*
[2]*Department of Physics, University of Helsinki, PO Box 64, FI-00014 Helsinki, Finland*
[3]*Independent researcher*
[4]*IRAP, CNRS, 9 avenue du Colonel Roche, BP 44346, F-31028 Toulouse Cedex 4, France*
[5]*Université de Toulouse, CNES, UPS-OMP, F-31028 Toulouse, France*
[6]*Center for Relativistic Astrophysics, School of Physics, Georgia Institute of Technology, 837 State Street, Atlanta, GA 30332-0430, USA*
[7]*European Space Agency, ESTEC, Keplerlaan 1, NL-2200 AG Noordwijk, the Netherlands*
[8]*Columbia Astrophysics Laboratory, Columbia University, 550 West 120th Street, New York, NY 10027, USA*
[9]*Institut für Astronomie und Astrophysik, Kepler Center for Astro and Particle Physics, Universität Tübingen, Sand 1, D-72076 Tübingen, Germany*

Accepted 2025 May 28. Received 2025 May 27; in original form 2025 March 27

ABSTRACT

Modelling the coherent pulsations observed during thermonuclear bursts offers a valuable method to probe the poorly understood equation of state of dense and cold matter. Here we apply the pulse profile modelling technique to the pulsations observed with *Rossi X-ray Timing Explorer* during the 2001 superburst of 4U 1636−536. By employing a single, uniform-temperature hotspot model with varying size and temperature, along with various assumptions for background/accretion contribution, we find that each assumption leads to different inferred mass, radius, and compactness constraints. This highlights the critical need to better understand the mass accretion rate enhancement/reduction during thermonuclear bursts to accurately model burst oscillation sources using pulse profile modelling.

Key words: dense matter – equation of state – stars: neutron – pulsars: general – pulsars: individual: 4U 1636−53 – X-rays: stars.

1 INTRODUCTION

Type I X-ray bursts are thermonuclear explosions on neutron stars (NSs) in low-mass X-ray binaries (LMXBs; see Galloway et al. 2020, for a recent review). These bursts result from the accumulation of hydrogen or helium from the companion star, which forms an ocean on the surface of the NS. As pressure and temperature build up at the base of the ocean, the conditions eventually reach a critical threshold, triggering runaway thermonuclear reactions (for reviews see Bildsten 1998; Keek & Heger 2016) which produce sudden and intense bursts of X-rays.

Stable hydrogen or helium burning, as well as these thermonuclear bursts, can leave behind a layer of carbon-rich ashes (Keek & Heger 2016). Over time, when the pressure and temperature at the base of this carbon layer become sufficiently high, another runaway thermonuclear reaction of carbon fusion can occur, leading to what are known as superbursts. Superbursts are bright X-ray events that typically last several hours (see in't Zand 2017, for a review) and release approximately 10^{42} erg (see e.g. Cumming & Bildsten 2001; Strohmayer & Brown 2002). These events have now been reported in 16 NSs (Alizai et al. 2023) and can be used to probe system properties.

Similar to the coherent pulsations (known as burst oscillations) observed in the light curves of Type I X-ray bursts (see Watts 2012; Bilous & Watts 2019, for a review), coherent pulsations have been observed in one superburst, from 4U 1636−536, during its cooling phase (Strohmayer & Markwardt 2002, hereafter SM02). These coherent pulsations are powerful tools for inferring the masses and radii of thermonuclear burst oscillation (TBO) sources (Bhattacharyya et al. 2005; Lo et al. 2013; Kini et al. 2023, 2024a,b) through the pulse profile modelling (PPM) technique.

PPM leverages both general and special relativistic effects to extract the NS properties encoded in the energy distribution and arrival times (rotational phase) of the observed photons. This technique has been employed to set constraints on the properties of rotation-powered millisecond pulsars (see e.g. Miller et al. 2019; Riley et al. 2019; Choudhury et al. 2024; Dittmann et al. 2024; Salmi et al. 2024a; Vinciguerra et al. 2024) using *Neutron Star Interior Composition Explorer* (Gendreau et al. 2016) data. These constraints have not only provided unprecedented insights into the equation of state of cold and dense matter (Raaijmakers et al. 2021; Annala et al. 2023; Takátsy et al. 2023; Zhu, Li & Liu 2023; Huang et al. 2024; Kurkela, Rajagopal & Steinhorst 2024; Pang et al. 2024; Rutherford et al.

★ E-mail: y.kini@uva.nl

© The Author(s) 2025.
Published by Oxford University Press on behalf of Royal Astronomical Society. This is an Open Access article distributed under the terms of the Creative Commons Attribution License (https://creativecommons.org/licenses/by/4.0/), which permits unrestricted reuse, distribution, and reproduction in any medium, provided the original work is properly cited.

Downloaded from https://academic.oup.com/mnras/article/541/1/46/8156801 by Universiteit van Amsterdam user on 23 March 2026

2024), but have also shed light on the surface properties of these stars' magnetic field structure (Bilous et al. 2019; Chen, Yuan & Vasilopoulos 2020; Kalapotharakos et al. 2021; Pétri et al. 2023).

Recent works (Kini et al. 2023, 2024a) have explored methods to accurately infer the properties of TBO sources using PPM of the pulsations observed during Type I X-ray bursts, employing the X-ray Pulse Simulation and Inference (X-PSI;[1] Riley et al. 2023) package. By dividing bursts into short-time segments and jointly modelling these segments, the systematic bias introduced by overlooking the short-scale time variability associated with these bursts and burst oscillations can be mitigated. A follow-up study (Kini et al. 2024b) applied these techniques to the burst oscillation source XTE J1814−338, yielding a mass of $1.21^{+0.05}_{-0.05}\,M_\odot$ and an equatorial radius of $7.0^{+0.4}_{-0.4}$ km. The small inferred radius, coupled with the challenge of explaining the harmonic content in the data, led the authors to suggest potential limitations (see section 4.5 of Kini et al. 2024b) with using the applied model(s). Nevertheless, this study was a useful step in the use of PPM for TBO sources, showing its potential for understanding the burst oscillation mechanism.

The properties of NSs inferred through PPM can be sensitive to the background limits imposed during sampling (Lo et al. 2013; Psaltis, Özel & Chakrabarty 2014; Salmi et al. 2022). In the context of PPM of TBO sources, 'background' refers to counts not originating directly from the stellar surface. This includes counts not caused by any astrophysical X-ray source, as well as counts from other X-ray sources within the field of view or within the LMXB system itself. Given that we do not yet model the accretion disc and (if present) any accretion column effect for TBO sources, photons originating from the accretion disc constitute the dominant background source. This presents a significant challenge in modelling TBO sources, as the contribution of accretion to the overall burst flux remains poorly constrained.

One approach to modelling burst spectra assumes that the accretion contribution during the burst has the same spectrum as the persistent emission, enhanced or reduced by a factor (`fa`; see Worpel, Galloway & Price 2013). The exact upper and lower limits on the scaling factor `fa` are hard to constrain a priori, as they depend on the sources and the burst. From burst spectral modelling, values up to $\texttt{fa} \approx 80$ have been obtained, and a reduction rather than an enhancement can also be expected ($\texttt{fa} \leq 1$; Worpel, Galloway & Price 2015; Degenaar et al. 2018). On the theoretical side, hydrodynamic simulations of the accretion disc's response to bursts have shown that mass accretion rates can increase by up to a factor of 10 in some cases (Fragile et al. 2018; Fragile, Ballantyne & Blankenship 2020; Speicher, Fragile & Ballantyne 2023; Speicher, Ballantyne & Fragile 2024). This enhancement is due to Poynting–Robertson drag, along with disc collapse driven by Compton cooling in the case of hot and geometrically thick accretion flows. However, Speicher et al. (2024) found that `fa` correlates more closely with the thermal temperature of the disc surface heated by the burst, rather than the mass accretion rate itself. This makes accurately modelling the accretion contribution during bursts particularly challenging. Further challenges may arise from the possibility that `fa` is spectrally dependent (Kajava et al. 2017).

In this work, we apply PPM to the pulsations observed with the *Rossi X-ray Timing Explorer*/Proportional Counter Array (*RXTE*/PCA; Jahoda et al. 1996) during the 2001 superburst of 4U 1636−536 to infer its properties. We follow the `fa` method to set limits on the accretion contribution during the superburst. Given that the scaling factor `fa` is difficult to determine a priori, we set an upper limit on `fa`, assuming various scenarios.

The rest of the paper is structured as follows. First, we discuss the modelling methodology, including the data and models used in Section 2. We present our results in Section 3. In Section 4, we explore interesting aspects of the results. Finally, we conclude in Section 5.

2 METHOD

The data and reduction methods for this analysis are outlined in Section 2.1. The model is detailed in Section 2.2 and includes the space–time framework in which the star is embedded, the surface emission, the background model, the atmosphere model, the interstellar medium (ISM) absorption model, and the instruments model.

2.1 Data

4U 1636−536 is a persistent accreting NS known for its prolific Type I X-ray bursting activity, with more than 600 normal Type I X-ray bursts (Galloway et al. 2020) along with four superbursts reported (Wijnands 2001; SM02; Kuulkers 2004, 2009). In this analysis, we focus on data from the superburst observed with *RXTE*/PCA on 2001 February 22, where pulsations were detected as reported by SM02. The light curve of this portion of the superburst is shown in the top panel of Fig. 1. The data collection for this superburst began at MJD 51962 (2001 February 22) and spans approximately 800 s. The observations were recorded in an event mode (E_125us_64M_0_1s) with 64 energy channels and a time resolution of 122 μs. The data were barycentred using the DE200 Solar system ephemeris with the `faxbary` tool from the HEASARC package.[2] The source coordinates were taken to be RA $= 16^{\rm h}40^{\rm m}55\overset{\rm s}{.}44$ and Dec. $= -53^\circ45'05\overset{''}{.}04$ (Galloway et al. 2020).

To find the frequency of pulsations, we computed Z^2 statistics (Buccheri et al. 1983) in 64-s windows starting every 16 s. As in SM02, for t_0 we adopted the barycentric equivalent of topocentric timestamp UTC 2001-02-22 17:02:25. Contours for Z^2 are shown in Fig. 2. The oscillation frequency undergoes visible linear drift over the course of 800 s. SM02 attributed this drift to the orbital motion of the NS and fitted it with the following expression:

$$\nu(t) = \nu_0 \left[1 - \frac{V_{\rm ns}\sin i}{c}\sin(2\pi(t-t_0)/P_{\rm orb} + 2\pi\phi_0)\right], \quad (1)$$

where ν_0 is the barycentric frequency, $V_{\rm ns}\sin i/c$ the projected neutron star velocity, ϕ_0 the fractions of the orbital phase at the start of the pulsation interval, and $P_{\rm orb}$ the orbital period.

Although our data set is the same as in SM02 and our analysis follows the one in their work closely, we found that the drift is best described by a slightly different combination of parameters, which were obtained by maximizing Z^2 statistics over a grid of trial values. The largest difference was found to be in ν_0, with our value of $\nu_0 = 582.1424$ Hz being 3 mHz lower. The other parameters adopted were as follows: $V_{\rm proj} = 135.2$, $\phi_0 = 0.292$. All of these values lie within the 90 per cent confidence levels of the fit from SM02. Similarly to SM02, we fixed the value of the orbital period at $P_{\rm orb} = 3.79316732$ h obtained from optical observations.

[1] https://github.com/xpsi-group/xpsi.git

[2] https://heasarc.gsfc.nasa.gov/

Downloaded from https://academic.oup.com/mnras/article/541/1/46/8156801 by Universiteit van Amsterdam user on 23 March 2026

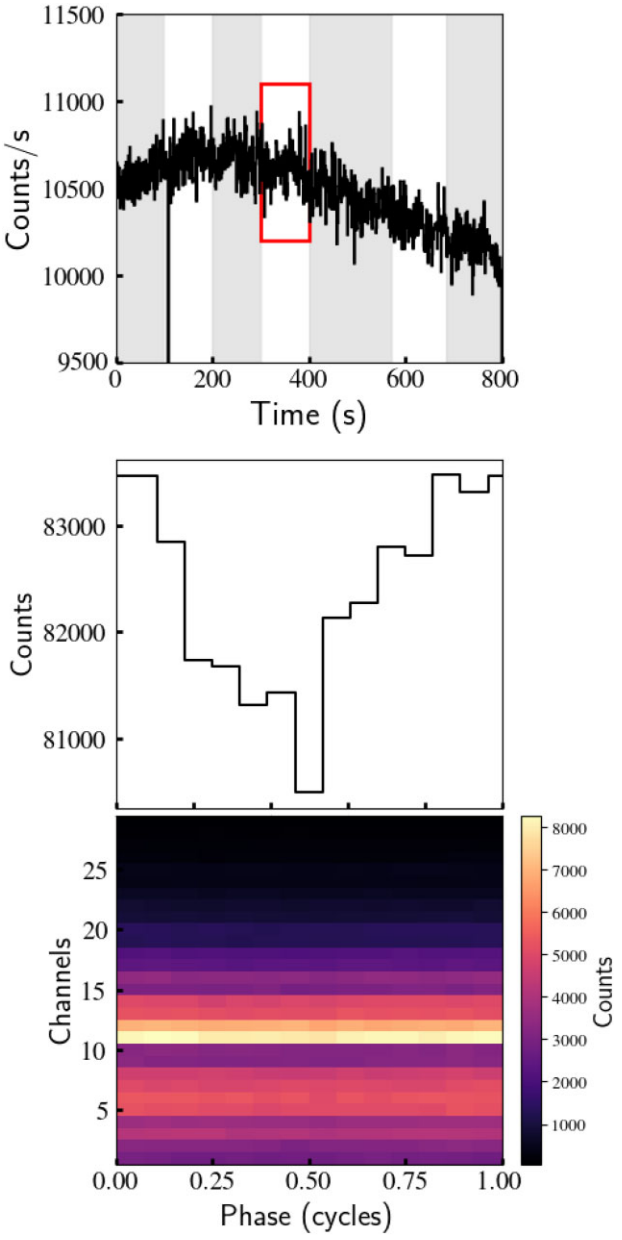

Figure 1. The portion of the light curve of 4U 1636−536 showing the burst oscillation (top panel). We note that the interval where the count rate drops below the panel range falls outside a good-time interval of *RXTE*, and its contribution is negligible. The grey and white vertical bands indicate the data slicing used for the analysis (see Section 2.2). The middle and bottom panels, respectively, show the pulse profile summed over the channel subset [1, 30] and the phase-folded pulse profile for Segment 4, which is highlighted in red (top panel). The rms FA of the pulse is approximately 0.7 per cent, which is very low.

Photon energies were calibrated with a response matrix created with the standard task `pcarsp` from the HEASARC package. For energy-resolved analysis, we selected data from the channel subset [1, 30], corresponding to a nominal photon energy range of [2.0, 26.5] keV as this range contains the majority of the observed counts (see Fig. 1). Background count rates were estimated from observations right before the burst start, conducted in the same mode as the main data file and calibrated with the same response matrix.

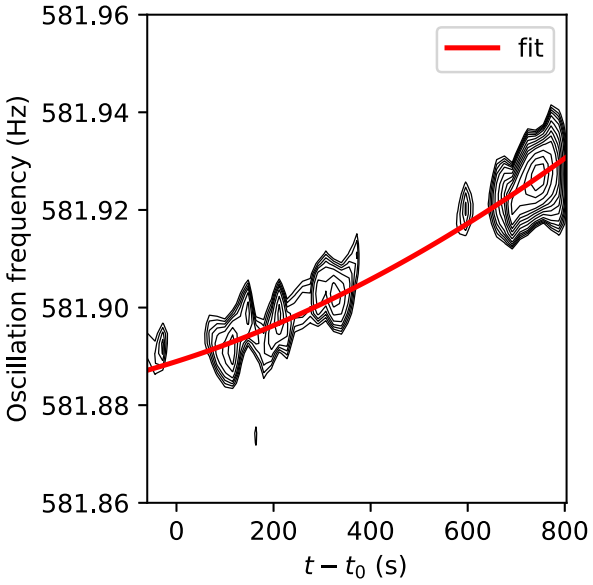

Figure 2. Dynamic Z^2 power spectrum for the data segment with pulsations. As in fig. 3 of SM02, Z^2 statistics were computed within 64-s time intervals starting every 16 s. Contour grids correspond to Z^2 of 16, 18, 20, 22, 25, 30, 35, 40, 45, 50, 60, 70, 80, and 90. Red line shows $\nu(t)$ from equation (1). Time is measured from t_0 at 17:02:25 UTC on 2001 February 22.

2.2 Model

The space–time model provides information on the mass and radius of the NS. In this work, we assume a Schwarzschild space–time while incorporating special relativistic effects and accounting for stellar oblateness due to rotation (see Poutanen & Gierliński 2003; Morsink et al. 2007; AlGendy & Morsink 2014; Bogdanov et al. 2019, for more detail). For the surface emission, we assume the coherent pulsations observed during the superburst were generated by a single, uniform-temperature hotspot. This model was identified by Artigue et al. (2013) as a viable option for modelling the oscillations observed during the superburst of 4U 1636−536. We also assume a non-zero temperature for the rest of the stellar surface, as the entire surface is expected to undergo burning during the superburst. To track the changes in pulse fraction observed in the data, we divided the superburst data set into seven different segments.[3] We allowed the hotspot temperature and angular radius to evolve independently across these segments. However, because the cooling is relatively slow during the superburst (see Fig. 1) and the pulsations occur only in a small portion of the cooling phase, we kept the temperature of the rest of the stellar surface non-variable across segments. Similarly, the phase shift was kept non-variable across segments, as the observed frequency drift arises from orbital motion rather than changes in the hotspot's location. For computational efficiency, we also kept the colatitude of the hotspot centre non-variable across segments.

We used the hot NS atmosphere model (solar composition) of Suleimanov, Poutanen & Werner (2012) to account for modifications to the spectrum and pulse shape as photons pass through the thin layer

[3]The light curve was divided into seven segments to reflect changes in rms FA over time while keeping the computational cost manageable. The first 400 s (see Fig. 2), with strong oscillations, were split into four 100-s segments. The low-amplitude interval from about 400 to 570 s was treated as a single segment, and the final portion, where oscillations re-emerge, was divided into two segments of approximately 150 s each.

Downloaded from https://academic.oup.com/mnras/article/541/1/46/8156801 by Universiteit van Amsterdam user on 23 March 2026

Table 1. List of all free parameters and their prior bounds used in this study.

Parameter	Description	Assumed prior
M ($M_\odot$)	Gravitational mass	$M \sim \mathcal{U}(1.0, 3.0)$
R_{eq} (km)	Equatorial radius	$R_{eq} \sim \mathcal{U}(3r_g(1.0), 16.0)^a$
D (kpc)	Distance	$D \sim \mathcal{U}(1.0, 20.0)$
$\cos(i)$	Cosine of the observer's inclination	$\cos(i) \sim \mathcal{U}(\cos(74^\circ), \cos(30^\circ))$
ϕ_{spot} (cycles)	Hotspot phase	$\phi_{spot} \sim \mathcal{U}(-0.25, 0.75)$
Θ_{spot} (rad)	Hotspot colatitude	$\cos(\Theta_{spot}) \sim \mathcal{U}(-1.0, 1.0)$
ζ_{spotX} (rad)	Hotspot angular radius	$\zeta_{spot} \sim \mathcal{U}(0.0, \pi/2)$
$\log[T_{spotX}(K)/1\,K]$	Hotspot temperature	$\log[T_{spot}(K)/1\,K] \sim \mathcal{U}(6.7, 7.6)$
$\log[T_{star}(K)/1\,K]$	Star temperature	$\log[T_{star}(K)/1\,K] \sim \mathcal{U}(6.7, 7.6)$
N_H (10^{20} cm^{-2})	ISM column density	$N_H \sim \mathcal{U}(15.0, 500.0)$ for `Case 0` $N_H \sim \mathcal{N}(30.0, 4.0^2)$ for `Case [1, 2, 3, 4, 5]`

[a] $r_g(1.0)$: solar Schwarzschild gravitational radius.

of atmosphere surrounding the NS. For the background model, we follow the standard procedure outlined in Section 1, using a range of `fa` values. Given the sensitivity of the results to the background limit, and thus the `fa` value, we considered six different scenarios. In `Case 0`, we set $1.5 \leq$ `fa` ≤ 2, consistent with the spectral modelling of Keek et al. (2014a). For the remaining cases, we set a more conservative threshold by using the instrument background as the lower limit. The upper limits were set as follows: `fa` $= [1, 2, 3, 4]$ for `Case [1, 2, 3, 4]`. Values greater than 4 lead to negligible differences, as the pre-burst counts, scaled by `fa`, become nearly identical or exceed the data in most channels. Therefore, we group all cases with `fa` values above 4 into a single scenario: `Case 5`. In this case, no upper limit is imposed on the background, allowing the background count rate to reach the observed data. This is a natural and agnostic choice when one lacks prior information about the background contribution to the total counts (see e.g. Riley et al. 2019).

To account for absorption in the ISM, we used the `Tbabs` model, which uses the photoelectric absorption cross-section from Wilms, Allen & McCray (2000). For `Case [1, 2, 3, 4, 5]`, we kept the interstellar attenuation column density, N_H, non-variable across all segments. However, for `Case 0`, we allowed N_H to vary between segments to facilitate comparison with the results of Keek et al. (2014a).

For inference, we set the spin frequency of the NS to 581.91 Hz (for each segment), which corresponds to the average barycentric oscillation frequency (see SM02). We also use the instrument response extracted as described in Section 2.1.

2.3 Priors

In Table 1, we provide a comprehensive list of all free parameters and their prior bounds used in this study. For the mass (M), equatorial radius (R_{eq}), hotspot phase (ϕ_{spot}), hotspot colatitude (Θ_{spot}), and hotspot angular radius (ζ_{spotX}, where X denotes the rank of the segment), we used the prior bounds as in previous PPM analyses (see e.g. Choudhury et al. 2024; Kini et al. 2024b; Salmi et al. 2024a; Vinciguerra et al. 2024). Detailed descriptions of the implicit priors affecting the joint (M, R_{eq}) prior space can be found in section 2.5 of Kini et al. (2023) and section 2.2.5 of Kini et al. (2024b).

For the observer's inclination ($\cos(i)$), we used the limits set by Casares et al. (2006) obtained from Doppler tomography in the optical waveband. The bounds of hotspot temperature (T_{spotX}) along with the star temperature (T_{star}) are set by the hot NS atmosphere model (see section 2.2 of Kini et al. 2023, for a detailed description).

For the distance (D) prior, we used a uniform distribution ranging from 1.0 to 20.0 kpc, despite existing distance prior knowledge about the optical companion star V801 Ara (Gaia Collaboration 2016; Bailer-Jones et al. 2021). This is because the geometric distance and the photogeometric distance, although broadly consistent, differ significantly from each other (see Fig. A1 in Appendix A). The potential reasons for this difference are legion and beyond the scope of this work.[4] Given the computational constraints of using each distance prior for all of the cases, we adopted a more conservative approach by using a uniform distribution. The bounds of this distribution were defined by the lowest value of the geometric distance samples and the highest value of the photogeometric distance samples.

For the ISM column density (N_H), we used bounds consistent with Keek et al. (2014a) for `Case 0` to facilitate comparison. For the remaining cases, we used bounds consistent with the values from H I maps of HI4PI Collaboration (2016) obtained with the `nH` tool.[5]

2.4 Posterior computation

To compute the posterior samples, we use MULTINEST (Feroz & Hobson 2008; Feroz, Hobson & Bridges 2009; Feroz et al. 2019) and PYMULTINEST (Buchner et al. 2014). For all the cases, we set the sampling efficiency and evidence tolerance to 0.3 and 0.1, respectively (for the definition of sampling efficiency and evidence tolerance, see Vinciguerra et al. 2023; Salmi et al. 2024a). For computational efficiency, we disabled the multimode/mode separation of MULTINEST. To determine the optimal number of live points, we randomly selected `Case 4` and performed inference with 8000 and 16 000 live points. As expected, the joint mass–radius posteriors broadened with an increased number of live points. However, the changes are not too large, and the 1D posteriors remained almost unchanged (see Fig. A2 in Appendix A). This provided confidence to proceed with 8000 live points for the remaining cases.

3 RESULTS

In this section, we primarily focus on the mass (M), radius (R_{eq}), and compactness (C),[6] given their importance for dense matter studies.

[4] Private discussion with Coryn Bailer-Jones. But some information can be found in Bailer-Jones et al. (2021) and at https://www2.mpia-hd.mpg.de/~calj/gedr3_distances/FAQ.html.

[5] https://heasarc.gsfc.nasa.gov/cgi-bin/Tools/w3nh/w3nh.pl

[6] $C = GM/R_{eq}c^2$, where G is the gravitational constant and c is the speed of light.

Downloaded from https://academic.oup.com/mnras/article/541/1/46/8156801 by Universiteit van Amsterdam user on 23 March 2026

However, the inferred properties of the hotspot for each case are also shown in Appendix A. We also summarize the main results presented in the section in Table 2.

The posterior distributions of mass, radius, and compactness obtained under each background assumption are shown in Fig. 3. The 2D contours represent the 68 per cent, 95 per cent, and 99 per cent credible regions, while the 1D plots on the diagonals display the marginalized posterior distributions (unnormalized) of each parameter. Each background assumption leads to significantly different mass and radius configurations, ranging from a low mass and small radius in `Case 5` to a large mass and radius in `Cases 0` and `2`. Interestingly, `Cases 3` and `4` yield similar results. Likewise, `Cases 0` and `2` yield similar results, with both mass and radius in these cases approaching the upper bounds of the prior parameter space. The resulting compactness also varies widely, from low compactness in `Case 1` to very high compactness in `Cases 0`, `2`, and `5`.

The uncertainties in the mass and radius for all cases except for `Case 5` are particularly small. The uncertainties on the equatorial radius – $\Delta R_{\rm eq}/R_{\rm eq}$ – are 0.5 per cent, 0.1 per cent, and 0.4 per cent, 10 per cent, and 5 per cent for `Case 0`, `Case 1`, `Case 2`, `Case 3`, and `Case 4`, respectively. Given that the total number of counts is approximately 8×10^6, with a background level of ∼6 per cent (in the most favourable scenario, `Case 1`), and a root-mean-square fractional amplitude (rms FA) of only ∼0.7 per cent, such low uncertainties are implausible. Even under highly idealized conditions – such as an equatorial hotspot viewed edge-on, assuming a radius of 15 km – the simplified estimation from Psaltis et al. (2014, equation 4) yields a lower limit on the radius uncertainty of approximately 15 per cent. This discrepancy suggests that a significant portion of the parameter vectors within the prior space are unable to adequately describe the data under these background constraints (see e.g. Kini et al. 2024a). This may indicate that the background assumptions for these cases do not accurately reflect the actual conditions during the superburst. Moreover, the evidence for these cases is worse compared to the other cases (see Table A1 in Appendix A), indicating that these background assumptions are not the preferred models.

In Fig. 4, we show the residual plot for each case for Segment 4 along with each residual distribution. Similar trends are observed in the other segments. Each residual distribution figure includes the p-value from the Kolmogorov–Smirnov (KS) test, which evaluates whether the distribution deviates from a normal distribution.

In `Cases 0` and `1`, distinct features appear in the residuals. In some channels, the model predicts significantly fewer counts than are observed in the data, indicated by horizontal red bands. Conversely, in other channels, the model predicts more counts than are observed, shown in blue. The distinct features in the residuals across both cases show that the model, under these background constraints, struggles to accurately match the observed data, either underestimating or overestimating the counts. The KS test yields a p-value of 3.28×10^{-8} in `Case 0`, showing that the residual distribution deviates significantly from normality. This is not unexpected, given that the residual distribution is bimodal, with the second mode caused by the model underestimating the observed counts in most channels. However, the p-value in `Case 1` indicates that the residuals are marginally consistent with a normal distribution. In the remaining cases, however, the residuals do not exhibit such distinct features, and their distributions are consistent with a Gaussian distribution (from the p-values).

The inferred background count rate for 200 samples randomly selected from the posterior distribution is shown in Fig. 5. In

Table 2. Summary of background assumptions, along with the inferred mass, inferred radius, inferred compactness, and key observations for each case. $c^k_{\rm pre\text{-}burst}$, $c^k_{\rm instr}$, and $c^k_{\rm model}$ represent the count rates in the kth energy channel for the pre-burst, the instrumental background, and the model, respectively.

Case	Background limit	M ($M_\odot$)	$R_{\rm eq}$(km)	C	Key results
0	$1.5c^k_{\rm pre\text{-}burst} + c^k_{\rm instr} \leq c^k_{\rm model} \leq 2c^k_{\rm pre\text{-}burst}$	$2.99^{+0.01}_{-0.02}$	$15.8^{+0.1}_{-0.1}$	$0.279^{+0.001}_{-0.001}$	Narrow posterior distributions Features in the residuals Residual distribution deviates from a normal distribution
1	$c^k_{\rm instr} \leq c^k_{\rm model} \leq c^k_{\rm pre\text{-}burst}$	$1.74^{+0.00}_{-0.00}$	$15.9^{+0.0}_{-0.0}$	$0.161^{+0.000}_{-0.000}$	Narrow posterior distributions Features in the residuals Residual distribution is consistent with a normal distribution
2	$c^k_{\rm instr} \leq c^k_{\rm model} \leq 2c^k_{\rm pre\text{-}burst}$	$2.99^{+0.01}_{-0.01}$	$15.8^{+0.1}_{-0.1}$	$0.279^{+0.001}_{-0.001}$	Narrow posterior distributions No features in the residuals Residual distribution is consistent with a normal distribution Inferred background remains below pre-burst level
3	$c^k_{\rm instr} \leq c^k_{\rm model} \leq 3c^k_{\rm pre\text{-}burst}$	$1.79^{+0.40}_{-0.38}$	$14.4^{+1.1}_{-1.7}$	$0.185^{+0.040}_{-0.030}$	Narrow posterior distributions No features in the residuals Residual distribution is consistent with a normal distribution
4	$c^k_{\rm instr} \leq c^k_{\rm model} \leq 4c^k_{\rm pre\text{-}burst}$	$1.77^{+0.22}_{-0.22}$	$15.1^{+0.6}_{-1.1}$	$0.178^{+0.014}_{-0.021}$	Narrow posterior distributions No features in the residuals Residual distribution is consistent with a normal distribution
5	$c^k_{\rm instr} \leq c^k_{\rm model} \leq c^k_{\rm data}$	$1.44^{+0.54}_{-0.30}$	$8.6^{+3.5}_{-1.9}$	$0.261^{+0.049}_{-0.064}$	No features in the residuals Residual distribution is consistent with a normal distribution Inferred background accounts for 95 per cent of observed counts in some segments

Downloaded from https://academic.oup.com/mnras/article/541/1/46/8156801 by Universiteit van Amsterdam user on 23 March 2026

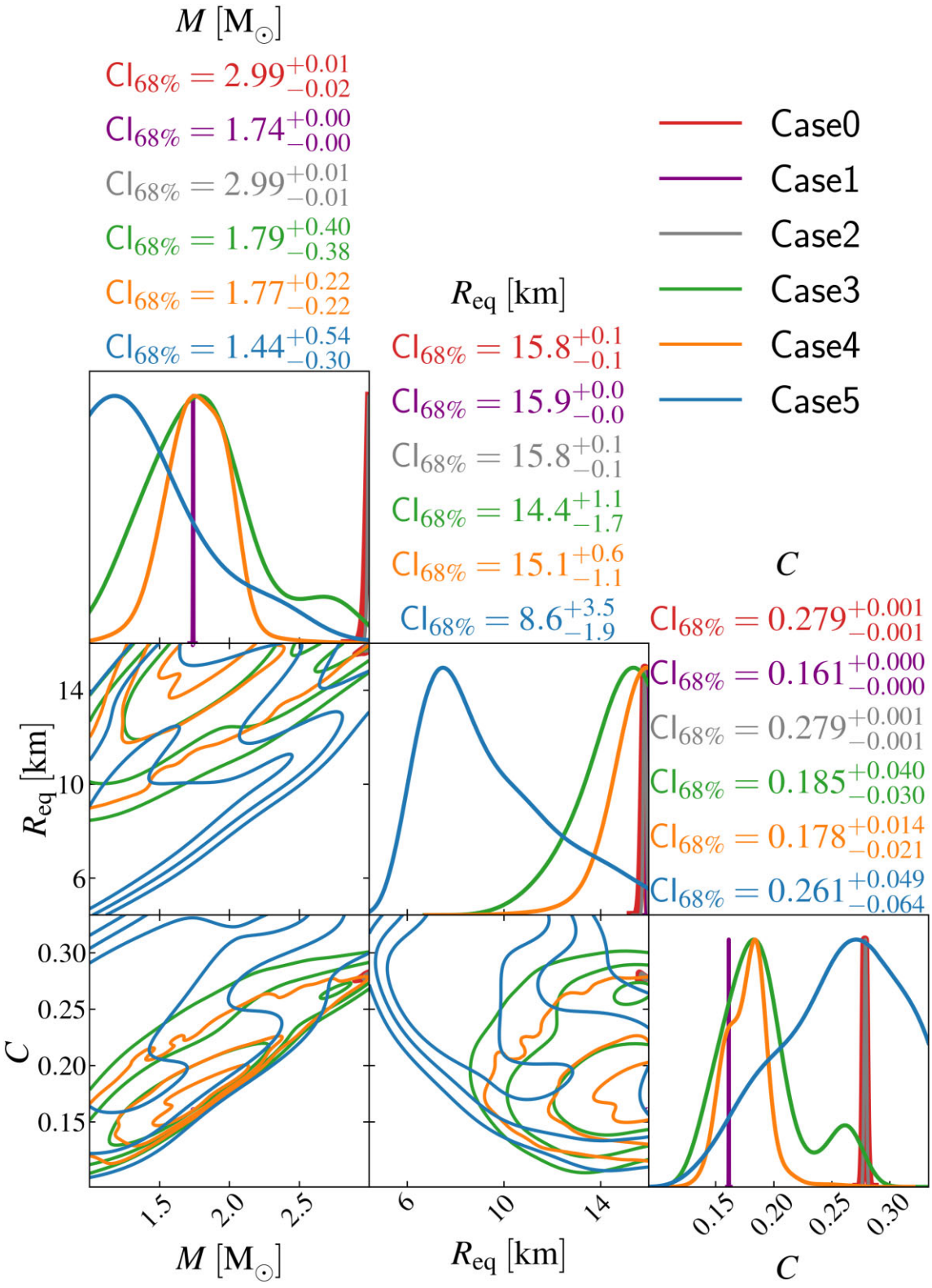

Figure 3. Posterior distributions of mass, radius, and compactness obtained under each background assumption. The 2D contours represent the 68 per cent, 95 per cent, and 99 per cent credible regions, while the 1D plots on the diagonals display the marginalized posterior distributions (unnormalized) of each parameter.

Downloaded from https://academic.oup.com/mnras/article/541/1/46/8156801 by Universiteit van Amsterdam user on 23 March 2026

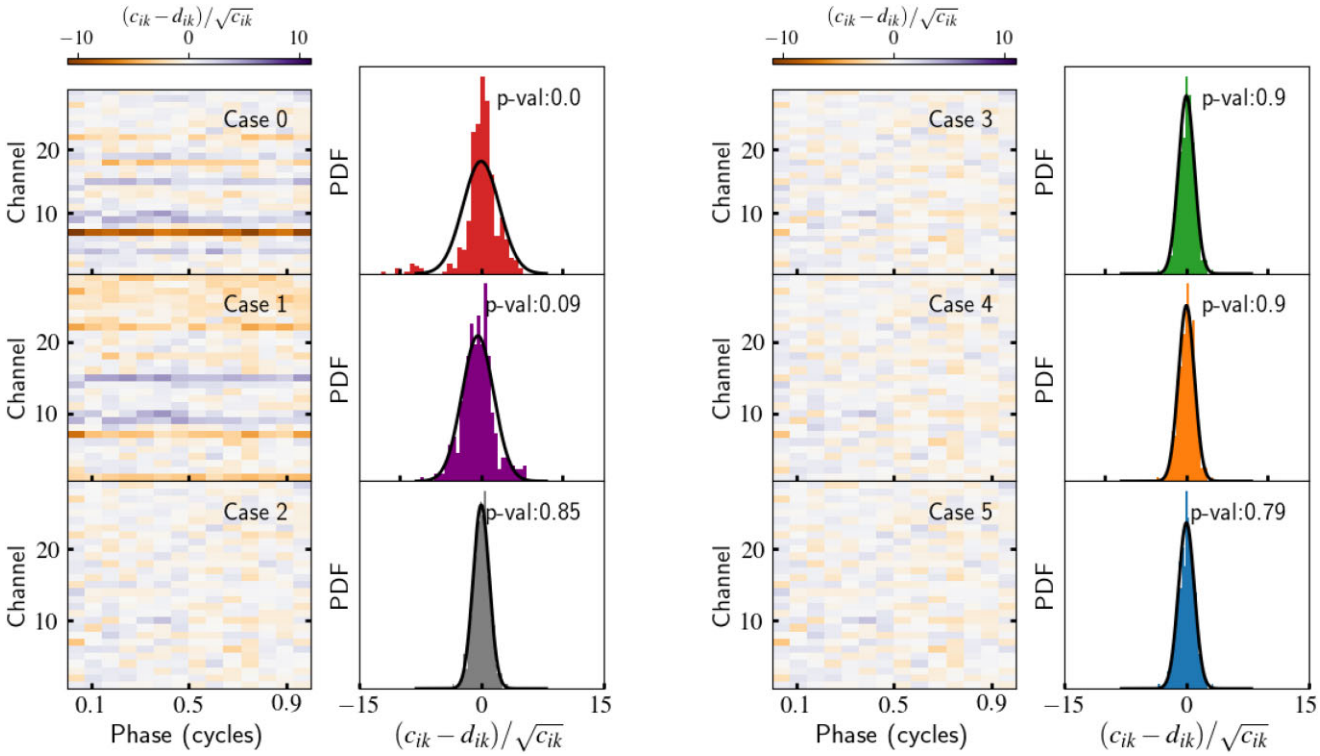

Figure 4. Residual plots and distributions for Segment 4 for each case. The solid black line in the distribution plots indicates the normal distribution that best fits the residual distribution. Each residual distribution plot shows the p-value from the KS test, assessing whether the residual distribution deviates from a normal distribution. c_{ik} and d_{ik} are, respectively, the model counts (signal averaged over 100 random samples from the posterior distribution) and the data counts in the ith rotation phase and kth energy channel.

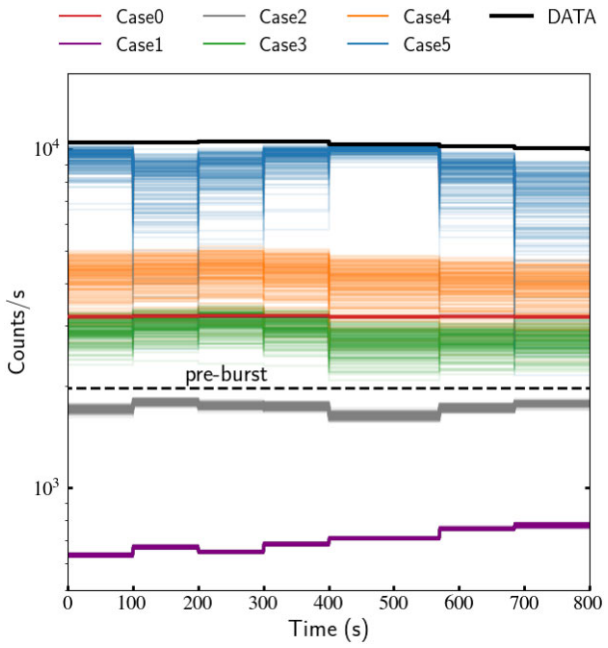

Figure 5. Inferred background count rate for 200 random samples, for each case alongside the observed data for each time segment. The 'inferred background' is the background spectrum that maximizes the likelihood for a given parameter vector. The horizontal black line indicates the pre-burst count rate.

both `Case 1` and `Case 2`, the inferred background remains below the pre-burst level (which is expected for `Case 1` and not necessarily for `Case 2`), indicated by the black dashed line. However, in `Case 5`, the inferred background is significantly higher, nearly matching the observed data in most segments. Specifically, for the maximum likelihood vector in `Case 5`, the inferred background count rate accounts for approximately 95 per cent of the actual data in Segment 5. This indicates that, in this case, a significant portion of the data are inferred to be background.

4 DISCUSSION

In this analysis, we used a single hotspot model along with various background assumptions – since the background levels and variation during a superburst are not known a priori – to infer the properties of 4U 1636−536. Our findings show that each background assumption resulted in distinct values for the inferred mass, radius, and compactness of 4U 1636−536. Similar results were obtained in the case of XTE J1814−338 (Kini et al. 2024b). These differences in compactness (hence in mass or radius) are not unexpected, as each background assumption inherently constrains the possible compactness of these sources. This is because for a given unpulsed component, setting a lower limit on the background implies that we allow the star to contribute more to the unpulsed component. This can be achieved by making the star more compact, ensuring that some part of the hotspot remains always visible to the observer due to gravitational lensing.

Downloaded from https://academic.oup.com/mnras/article/541/1/46/8156801 by Universiteit van Amsterdam user on 23 March 2026

4.1 `Case 0`

In `Case 0`, the distinct features in the residuals, the extremely narrow posterior distributions, and the deviation of the residual distribution from the expected Gaussian profile suggest that the models used (the single hotspot model along with the other models described in Section 2.2) may not be sufficient to describe the data, assuming the background limits found in Keek et al. (2014a) accurately reflect the true background. This inadequacy mirrors findings for XTE J1814−338 (Kini et al. 2024b). It indicates the probable need to incorporate additional components that can give rise to spectral lines, such as an accretion disc, into the model. During the superburst, intense X-rays emitted from the stellar surface illuminate the accretion disc, causing a significant portion of these X-rays to reflect off the disc. This reflection resulted in emission and absorption lines, along with reflection components, all of which have been identified in the data (Keek et al. 2014a). While adding these components might help explain the data at lower energy channels – particularly below Channel 15, as the iron line appears around 6.5 keV and iron edges near 9 keV (Keek et al. 2014a; Koljonen, Kajava & Kuulkers 2016) – they may not address the discrepancies observed in higher channels. Additionally, the pronounced feature in Channel 7 may not indicate an issue with that specific channel but rather a missing component in our model. This is because count excess and deficit can appear and disappear in different channels as more components are added, as found in the superburst spectral modelling of 4U 1636−536(see fig. 1 in Keek et al. 2014a).

4.2 `Cases 1 and 2`

In `Case 1`, the features in the residuals and their distribution indicate poor model performance under this background assumption. While the residuals and p-values in `Case 2` suggest that the model performs reasonably well under this background assumption, the extremely small parameter space regions that can explain the data in both `Case 1` and `Case 2` suggest that these background assumptions might not accurately capture the true physics (see Kini et al. 2024a). Moreover, in `Case 2`, most samples yield an inferred background below the pre-burst level, even though the background was allowed to reach up to twice the pre-burst level. This suggests that the likelihood hypervolumes explored in both cases are similar, with each solution representing just one mode of the likelihood hypervolume. The extremely small credible regions in both cases further indicate that the live points may have been stuck in local maxima during the runs.[7] Given this, the likelihood surface is likely multimodal, making it desirable to perform the runs with the multimode of MULTINEST enabled, using more live points. However, due to current computational constraints, we were unable to explore runs with more live points or enable the multimode option in MULTINEST.

In both cases, the inferred background remains below the pre-burst level, which could imply a decrease in the accretion rate during the superburst, at least over the time interval considered in this analysis. However, given the features in the residuals in `Case 1` and the extremely narrow posterior distributions in both cases, it is highly unlikely that the accretion rate decreased during the superburst.

[7]We also note that `Case 1` missed the better fitting `Case 2` solution (which is within the `Case 1` prior space). This implies that the live points were stuck for that case.

4.3 `Cases 3 and 4`

The lack of clustering in the residuals and the fact that the residual distributions are consistent with a Gaussian distribution in `Cases 3` and `4` suggest that setting a high upper limit on the background results in a better fit. This is because, in the background treatment in X-PSI, an excess or deficit of counts in a given channel in the model can be adjusted through background marginalization (see appendix B.2 of Riley 2019), as long as this excess or deficit falls within the bounds set on the expected background from the source. During a burst, an increase in the mass accretion rate by up to a factor of 4 can be expected (Fragile et al. 2018, 2020; Speicher et al. 2023, 2024). While the radius uncertainties obtained in `Cases 3` and `4` are larger than those in `Cases 0`, `1`, and `2`, they still remain below the idealized lower limit estimated in Section 3. This suggests that, despite the improved fit, the results obtained under these background assumptions may still underestimate the true uncertainties and are therefore unlikely to represent the true physical solution.

4.4 `Case 5`

In `Case 5`, an excess or deficit of counts in a given channel in the model can be adjusted through background marginalization similar to `Cases 3` and `4`. This explains the lack of clustering in the residuals. The inferred uncertainty on the radius is approximately 30 per cent, which is substantially larger than the idealized lower limit derived in Section 3. However, the inferred background is extremely high, reaching up to 95 per cent of the total observed counts in Segment 5. This result is inconsistent with the current burst model. During a superburst, most photons are expected to originate from nuclear burning on the stellar surface rather than from a simple enhancement of accretion (in't Zand 2017).

4.5 Caveats

The background limits explored in this paper struggled to explain the data, in part due to several simplifying assumptions made throughout our analysis. One important caveat in our modelling is the assumption that the entire stellar surface is visible. However, since 4U 1636−536 is not an accretion-powered pulsar, it is highly likely that the accretion disc is in contact with the stellar surface, potentially obscuring a significant portion of the star (Keek et al. 2014b). In future analyses, we plan to incorporate the effects of the accretion disc on the observed X-ray spectrum, including emission and absorption lines, as well as reflection components.

Other simplifications may also affect our inferences. These include assuming a single hotspot with a fixed shape and colatitude across all segments, as well as a uniform temperature across the spot and stellar surface. These assumptions could lead to systematic differences in background inference and, consequently, in mass and radius estimates. Future extensions could explore multiple spots, non-circular spot shapes (e.g. r-modes; Heyl 2004; Lee 2004; Piro & Bildsten 2005; Chambers et al. 2019; Chambers & Watts 2020), and temperature gradients across the hotspot/stellar surface. However, these additions will significantly increase computational costs and are left for future work.

Another limitation arises from our choice of segmenting the superburst light curve into seven time intervals. While this scheme was designed to capture the observed variation in pulse amplitude (see Figs 1 and 2) and to keep the parameter space tractable, it remains possible that the segmentation itself introduces biases. We did not systematically explore alternative segmentation strategies due

Downloaded from https://academic.oup.com/mnras/article/541/1/46/8156801 by Universiteit van Amsterdam user on 23 March 2026

to computational constraints, and thus the sensitivity of our results to the chosen scheme remains an open question.

Finally, a further limitation comes from disabling MULTINEST multimode functionality, which may have resulted in live points becoming trapped in local maxima. Additionally, the parameter space exploration might not have been thorough enough, leading to different solutions for different cases – a challenge similar to that encountered in Salmi et al. (2024b) during PPM on PSR J1231−1411. While increasing the number of live points and reducing MULTINEST's sampling efficiency could potentially mitigate this issue, it comes with significantly increased computational costs. Given that the current runs already require substantial computation time (about 1.52×10^6 core hours for all the runs), further optimization presents a considerable challenge.

Although incorporating additional physical effects – such as non-circular spot shapes, disc occultation, reflection, etc. – would increase model complexity and the number of free parameters, we argue that the primary limitation is not the data quality. The data set contains approximately 8×10^6 counts, which is significantly more than those used in previous PPM analyses of rotation-powered pulsars (see e.g. Choudhury et al. 2024; Dittmann et al. 2024; Salmi et al. 2024a; Vinciguerra et al. 2024). Even if only a small fraction of this emission originates from the hotspot, this still represents a sufficient number of counts to allow for meaningful constraints. Instead, we find that the dominant limitations arise from astrophysical uncertainties, particularly in the background modelling, and from the computational cost of exploring high-dimensional parameter spaces.

5 CONCLUSION

In this study, we applied PPM to the pulsations observed during the 2001 superburst of 4U 1636−536, exploring various background assumptions to infer the mass, radius, and compactness of the NS. Our findings show that the inferred properties are highly sensitive to the background assumptions, resulting in significant variations across different scenarios. This underscores the critical need for a more accurate understanding of the background contributions during thermonuclear bursts to improve the reliability of PPM analyses of burst oscillations.

For `Cases 0` and `1`, features in the residuals and the small credible regions suggest that the corresponding background assumptions do not accurately reflect the physical conditions during the superburst. `Cases 2`, `3`, `4`, and `5` yield better fits, as indicated by improved residuals and p-values. However, in `Cases 2`, `3`, and `4`, the credible intervals remain significantly narrower than expected, indicating that these background assumptions also fail to fully capture the underlying physics. In `Case 5`, although the fit also improves, the inferred background level is extremely high – reaching up to 95 per cent of the total observed counts – which is inconsistent with the current understanding of superburst emission, where most of the observed flux is expected to originate from nuclear burning on the stellar surface.

The challenges in explaining the data under the background assumptions explored in this paper may stem from several assumptions discussed in Section 4.5. Looking ahead, we aim to adopt more sophisticated models for the accretion disc and its interactions with the NS during superbursts. A key challenge will be gaining a clearer understanding of the accretion contribution during thermonuclear bursts, which is essential for accurately inferring the properties of burst oscillation sources using PPM. Another promising direction would be to constrain the mass and radius prior space by using an equation of state – informed prior, similar to the approach in Salmi et al. (2024b). Furthermore, obtaining independent and reliable constraints from burst spectra modelling (e.g. Suleimanov et al. 2011, 2012, 2017; Özel 2013; Steiner, Lattimer & Brown 2013; Guillot & Rutledge 2014; Nättilä et al. 2016, 2017; Steiner et al. 2018; Molkov et al. 2024) or burst property modelling (e.g. Goodwin et al. 2021; Galloway et al. 2024) could greatly aid in constraining either the mass and radius or the superburst and the burst oscillation properties. Additionally, future work may benefit from leveraging more efficient inference techniques or machine learning-based surrogate models (see e.g. Miller et al. 2022; Boelts et al. 2025) to reduce computational costs. These developments could eventually make it feasible to explore more complex surface patterns and jointly model multiple bursts or superbursts from 4U 1636−536, under the assumption of shared intrinsic parameters such as mass, radius, distance, etc. Such a joint approach could, in principle, yield tighter constraints by mitigating source-intrinsic degeneracies and background-related uncertainties that affect individual burst analyses.

Traditionally, the accretion contribution during bursts is modelled by scaling the persistent emission by a factor, `fa`. In the hard state, the increased X-ray burst emission alters the spectral properties of the accretion disc (Kajava et al. 2017), suggesting that `fa` may be energy dependent – a factor we did not account for in this analysis. Additionally, a recent study by Speicher et al. (2024) indicates that `fa` correlates more strongly with the thermal temperature of the disc surface than with the mass accretion rate, complicating efforts to constrain the background. Identifying reliable tracers of the mass accretion rate through numerical simulations will be crucial for improving these constraints. This, in turn, will enhance our ability to probe the properties of dense matter and may provide new insights into the origin of burst oscillations.

ACKNOWLEDGEMENTS

We are grateful to the anonymous referee for their thoughtful comments and constructive suggestions, which helped improve the clarity and depth of the paper. We also thank Coryn Bailer-Jones for the discussion on distance priors and Tod E. Strohmayer for insightful discussions and feedback on the manuscript. This research made use of the national computing facilities subsidized by the Dutch Research Council (NWO) Domain Science. The majority of the computations were performed on the HELIOS cluster, exclusively on dedicated nodes funded through the European Research Council (ERC) Consolidator Grant No. 865768 AEONS (PI: Watts). YK, ALW, TS, and SV acknowledge support from this ERC Consolidator Grant. DRB acknowledges support from NASA award 80NSSC24K0212 and NSF grant AST-2407658.

DATA AVAILABILITY

All data, including posterior samples, as well as the scripts used for the analyses, runs, and plots, are publicly available on Zenodo (https://doi.org/10.5281/zenodo.14850910).

REFERENCES

AlGendy M., Morsink S. M., 2014, ApJ, 791, 78
Alizai K. et al., 2023, MNRAS, 521, 3608
Annala E., Gorda T., Hirvonen J., Komoltsev O., Kurkela A., Nättilä J., Vuorinen A., 2023, Nat. Commun., 14, 8451
Artigue R., Barret D., Lamb F. K., Lo K. H., Miller M. C., 2013, MNRAS, 433, L64

Downloaded from https://academic.oup.com/mnras/article/541/1/46/8156801 by Universiteit van Amsterdam user on 23 March 2026

Bailer-Jones C. A. L., Rybizki J., Fouesneau M., Demleitner M., Andrae R., 2021, AJ, 161, 147
Bhattacharyya S., Strohmayer T. E., Miller M. C., Markwardt C. B., 2005, ApJ, 619, 483
Bildsten L., 1998, in Buccheri R., van Paradijs J., Alpar M. A., eds, NATO Advanced Study Institute C (ASIC) Vol. 515, The Many Faces of Neutron Stars. Kluwer, Dordrecht, p. 419
Bilous A. V., Watts A. L., 2019, ApJS, 245, 19
Bilous A. V. et al., 2019, ApJ, 887, L23
Boelts J. et al., 2025, J. Open Source Softw., 10, 7754
Bogdanov S. et al., 2019, ApJ, 887, L26
Buccheri R. et al., 1983, A&A, 128, 245
Buchner J. et al., 2014, A&A, 564, A125
Casares J., Cornelisse R., Steeghs D., Charles P. A., Hynes R. I., O'Brien K., Strohmayer T. E., 2006, MNRAS, 373, 1235
Chambers F. R. N., Watts A. L., 2020, MNRAS, 491, 6032
Chambers F. R. N., Watts A. L., Keek L., Cavecchi Y., Garcia F., 2019, ApJ, 871, 61
Chen A. Y., Yuan Y., Vasilopoulos G., 2020, ApJ, 893, L38
Choudhury D. et al., 2024, ApJ, 971, L20
Cumming A., Bildsten L., 2001, ApJ, 559, L127
Degenaar N. et al., 2018, Space Sci. Rev., 214, 15
Dittmann A. J. et al., 2024, ApJ, 974, 295
Feroz F., Hobson M. P., 2008, MNRAS, 384, 449
Feroz F., Hobson M. P., Bridges M., 2009, MNRAS, 398, 1601
Feroz F., Hobson M. P., Cameron E., Pettitt A. N., 2019, Open J. Astrophys., 2, 10
Fragile P. C., Ballantyne D. R., Maccarone T. J., Witry J. W. L., 2018, ApJ, 867, L28
Fragile P. C., Ballantyne D. R., Blankenship A., 2020, Nat. Astron., 4, 541
Gaia Collaboration, 2016, A&A, 595, A1
Galloway D. K. et al., 2020, ApJS, 249, 32
Galloway D. K., Goodwin A. J., Hilder T., Waterson L., Cupák M., 2024, MNRAS, 535, 647
Gendreau K. C. et al., 2016, in den Herder J.-W. A., Takahashi T., Bautz M., eds, Proc. SPIE Conf. Vol. 9905, Space Telescopes and Instrumentation 2016: Ultraviolet to Gamma Ray. SPIE, Bellingham, p. 99051H
Goodwin A. J., Heger A., Chambers F. R. N., Watts A. L., Cavecchi Y., 2021, MNRAS, 505, 5530
Guillot S., Rutledge R. E., 2014, ApJ, 796, L3
Heyl J. S., 2004, ApJ, 600, 939
HI4PI Collaboration, 2016, A&A, 594, A116
Huang C., Raaijmakers G., Watts A. L., Tolos L., Providência C., 2024, MNRAS, 529, 4650
in't Zand J., 2017, in Serino M., Shidatsu M., Iwakiri W., Mihara T., eds, Understanding superbursts, 7 years of MAXI: Monitoring X-ray Transients. p. 121
Jahoda K., Swank J. H., Giles A. B., Stark M. J., Strohmayer T., Zhang W., Morgan E. H., 1996, in Siegmund O. H., Gummin M. A., eds, Proc. SPIE Conf. Vol. 2808, EUV, X-Ray, and Gamma-Ray Instrumentation for Astronomy VII. SPIE, Bellingham, p. 59
Kajava J. J. E., Sánchez-Fernández C., Kuulkers E., Poutanen J., 2017, A&A, 599, A89
Kalapotharakos C., Wadiasingh Z., Harding A. K., Kazanas D., 2021, ApJ, 907, 63
Keek L., Heger A., 2016, MNRAS, 456, L11
Keek L., Ballantyne D. R., Kuulkers E., Strohmayer T. E., 2014a, ApJ, 789, 121
Keek L., Ballantyne D. R., Kuulkers E., Strohmayer T. E., 2014b, ApJ, 797, L23
Kini Y. et al., 2023, MNRAS, 522, 3389
Kini Y. et al., 2024a, MNRAS, 527, 8118
Kini Y. et al., 2024b, MNRAS, 535, 1507
Koljonen K. I. I., Kajava J. J. E., Kuulkers E., 2016, ApJ, 829, 91
Kurkela A., Rajagopal K., Steinhorst R., 2024, Phys. Rev. Lett., 132, 262701
Kuulkers E., 2004, Nucl. Phys. B: Proc. Suppl., 132, 466
Kuulkers E., 2009, Astron. Telegram, 2140, 1
Lee U., 2004, ApJ, 600, 914
Lo K. H., Coleman Miller M., Bhattacharyya S., Lamb F. K., 2013, ApJ, 776, 19
Miller M. C. et al., 2019, ApJ, 887, L24
Miller B. K., Cole A., Weniger C., Nattino F., Ku O., Grootes M. W., 2022, J. Open Source Softw., 7, 4205
Molkov S. V. et al., 2024, A&A, 690, A353
Morsink S. M., Leahy D. A., Cadeau C., Braga J., 2007, ApJ, 663, 1244
Nättilä J., Steiner A. W., Kajava J. J. E., Suleimanov V. F., Poutanen J., 2016, A&A, 591, A25
Nättilä J., Miller M. C., Steiner A. W., Kajava J. J. E., Suleimanov V. F., Poutanen J., 2017, A&A, 608, A31
Özel F., 2013, Rep. Prog. Phys., 76, 016901
Pang P. T. H., Sivertsen L., Somasundaram R., Dietrich T., Sen S., Tews I., Coughlin M. W., Van Den Broeck C., 2024, Phys. Rev. C, 109, 025807
Pétri J. et al., 2023, A&A, 680, A93
Piro A. L., Bildsten L., 2005, ApJ, 629, 438
Poutanen J., Gierliński M., 2003, MNRAS, 343, 1301
Psaltis D., Özel F., Chakrabarty D., 2014, ApJ, 787, 136
Raaijmakers G. et al., 2021, ApJ, 918, L29
Riley T. E., 2019, PhD thesis, Univ. Amsterdam, Amsterdam. https://hdl.handle.net/11245.1/aa86fcf3-2437-4bc2-810e-cf9f30a98f7a, last access date: June 21st, 2025
Riley T. E. et al., 2019, ApJ, 887, L21
Riley T. E. et al., 2023, J. Open Source Softw., 8, 4977
Rutherford N. et al., 2024, ApJ, 971, L19
Salmi T. et al., 2022, ApJ, 941, 150
Salmi T. et al., 2024a, ApJ, 974, 294
Salmi T. et al., 2024b, ApJ, 976, 58
Speicher J., Fragile P. C., Ballantyne D. R., 2023, MNRAS, 526, 1388
Speicher J., Ballantyne D. R., Fragile P. C., 2024, ApJ, 976, 44
Steiner A. W., Lattimer J. M., Brown E. F., 2013, ApJ, 765, L5
Steiner A. W., Heinke C. O., Bogdanov S., Li C. K., Ho W. C. G., Bahramian A., Han S., 2018, MNRAS, 476, 421
Strohmayer T. E., Brown E. F., 2002, ApJ, 566, 1045
Strohmayer T. E., Markwardt C. B., 2002, ApJ, 577, 337 (SM02)
Suleimanov V., Poutanen J., Revnivtsev M., Werner K., 2011, ApJ, 742, 122
Suleimanov V., Poutanen J., Werner K., 2012, A&A, 545, A120
Suleimanov V. F., Poutanen J., Nättilä J., Kajava J. J. E., Revnivtsev M. G., Werner K., 2017, MNRAS, 466, 906
Takátsy J., Kovács P., Wolf G., Schaffner-Bielich J., 2023, Phys. Rev. D, 108, 043002
Vinciguerra S., Salmi T., Watts A. L., Choudhury D., Kini Y., Riley T. E., 2023, ApJ, 959, 55
Vinciguerra S. et al., 2024, ApJ, 961, 62
Watts A. L., 2012, ARA&A, 50, 609
Wijnands R., 2001, ApJ, 554, L59
Wilms J., Allen A., McCray R., 2000, ApJ, 542, 914
Worpel H., Galloway D. K., Price D. J., 2013, ApJ, 772, 94
Worpel H., Galloway D. K., Price D. J., 2015, ApJ, 801, 60
Zhu Z., Li A., Liu T., 2023, ApJ, 943, 163

APPENDIX A: PRIORS, POSTERIORS, AND EVIDENCE ANALYSIS

Fig. A1 shows the geometric and photogeometric distance distribution derived from *Gaia* Data Release 3 (Gaia Collaboration 2016; Bailer-Jones et al. 2021) (not used in this work), alongside the uniform prior used in this work (hot pink dashed line) and the inferred posterior distributions. Note that the distributions are not normalized.[8] Although the geometric and photogeometric distance distributions differ significantly, they remain broadly consistent. In `Cases 0` and `2`, the inferred posterior distributions are only

[8]The area under the curve is not necessarily equal to 1.

Downloaded from https://academic.oup.com/mnras/article/541/1/46/8156801 by Universiteit van Amsterdam user on 23 March 2026

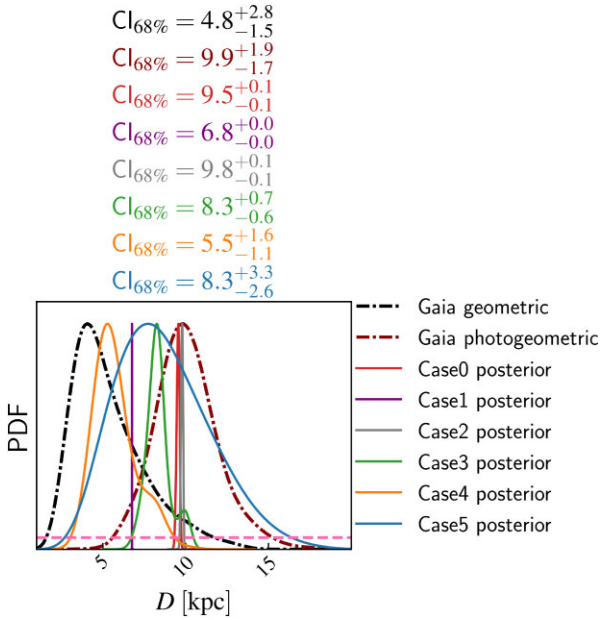

Figure A1. Comparison of the *Gaia* geometric and photogeometric distances (not used in this work) with the inferred posterior distribution for each case. The uniform prior used in this study is shown by the hot pink dashed line.

marginally consistent with the *Gaia* geometric distance distribution, intersecting only at the tail of the distribution. In `Case 1`, the inferred distribution is marginally consistent with the *Gaia* photogeometric distance distribution. However, in the remaining cases, the inferred distributions are consistent with both the geometric and photogeometric distance distributions.

In Fig. A2, we show the posterior distributions of mass, radius, and compactness computed with varying numbers of live points for `Case 4`. The posterior distributions for the remaining parameters are available on Zenodo (https://doi.org/10.5281/zenodo.14850910). The joint mass–radius posteriors became broader with more live points. However, the 1D posteriors remained largely unaffected. A similar trend can be seen (see Zenodo) for the remaining parameters, which reinforced our confidence in using 8000 live points for the remaining cases.

We report in Table A1 the nested sampling global ln-evidence for each background assumption. Based on the ln-evidence, `Case 4` emerges as the best model. However, the difference in ln-evidence between `Case 4` and `Case 3` or `Case 5` is minimal (only 10 in natural logarithmic units). This indicates that the models are almost indistinguishable in their ability to explain the data.

Fig. A3 shows the inferred evolution of the temperature and angular radius of the hotspot during the superburst. In most cases (except `Case 2`), the inferred temperature of the hotspot remains generally constant throughout the superburst. In `Case 1`, the angular radius of the hotspot also stays constant during the superburst. Therefore, it is not surprising why `Case 1` struggles to explain the data, given that the observed rms FA varies during the burst.

For the other cases, except `Cases 0` and `1`, a general trend is observed in the hotspot's angular radius. It stays relatively stable (within the 68 per cent level) during the initial part of the burst, then decreases before increasing again over time. This trend aligns with the observed rms FA and implies that the variation in the rms FA is due to changes in the hotspot's angular radius.

If 4U 1636−536 is indeed accreting via a boundary layer, then changes in the hotspot size might be attributed to the accretion disc

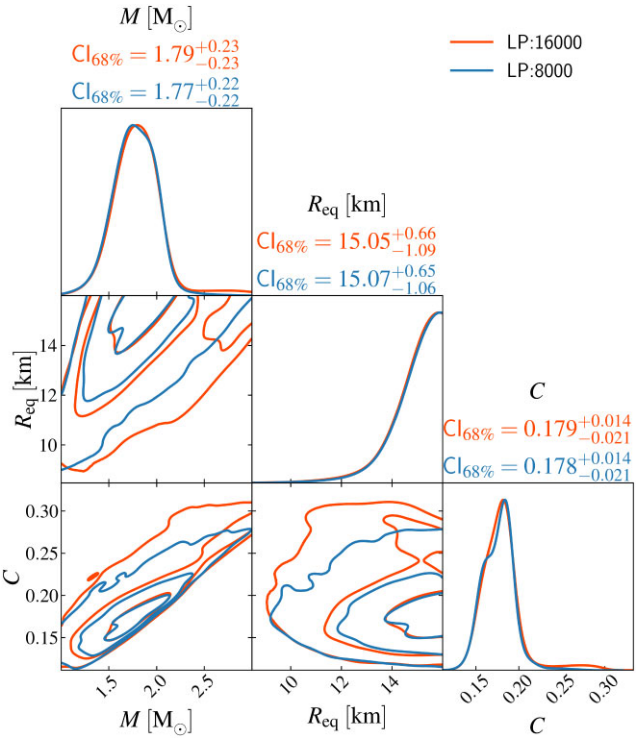

Figure A2. Posterior distributions of mass, radius, and compactness computed using varying numbers of live points (`Case 4`).

Table A1. Nested sampling global ln-evidence for each background assumption.

Case	ln-evidence ($\times 10^5$)
`Case 0`	−0.2108
`Case 1`	−0.1923
`Case 2`	−0.1435
`Case 3`	−0.1422
`Case 4`	−0.1421
`Case 5`	−0.1422

wobbling during the superburst. This wobble could make parts of the hotspot more or less visible over time. However, it remains uncertain whether a disc could wobble over such a short time-scale. Another possible explanation is that the disc itself pulsates (e.g. the inner disc

Downloaded from https://academic.oup.com/mnras/article/541/1/46/8156801 by Universiteit van Amsterdam user on 23 March 2026

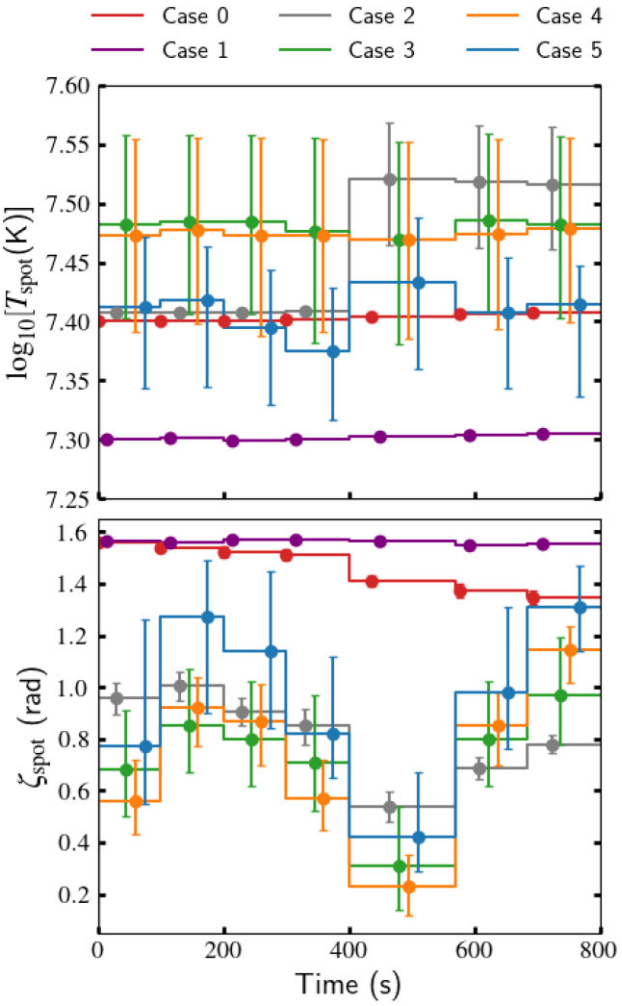

Figure A3. Median of the inferred temperature and angular radius of the hotspot. The error bars are the 68 per cent uncertainty regions.

moving in and out) during the superburst, though this seems unlikely since the burst was not a pre-burst (Keek et al. 2014a). Alternatively, the inner accretion disc, depleted at the start of the burst, could be replenished, making the inner disc more opaque and thus causing the hotspot to become less visible at certain points during the burst, and more visible again if the inner disc depletes once more. However, replenishment would imply an increase in the accretion rate, which should correspond to a rise in the inferred background during that period. However, this scenario is unlikely as the inferred background generally remains constant for most cases.

This paper has been typeset from a TEX/LATEX file prepared by the author.

Downloaded from https://academic.oup.com/mnras/article/541/1/46/8156801 by Universiteit van Amsterdam user on 23 March 2026

© The Author(s) 2025.
Published by Oxford University Press on behalf of Royal Astronomical Society. This is an Open Access article distributed under the terms of the Creative Commons Attribution License (https://creativecommons.org/licenses/by/4.0/), which permits unrestricted reuse, distribution, and reproduction in any medium, provided the original work is properly cited.